Evaluation of pinnacle reef distribution at shallow subsurface using integrated geophysical methods: a case study from the Upper Kimmeridgian (Spain)

Ó. Pueyo Anchuela [a*], G. San Miguel [b], B. Bádenas [a], M. Aurell [a]

[a] Departamento de Ciencia de la Tierra, Universidad de Zaragoza, C/Pedro Cerbuna 12, 50009, Zaragoza, Spain; opueyo@unizar.es (*corresponding author), bbadenas@unizar.es, maurell@unizar.es

[b] Total E&P, Technology Centre, CSTJF, Avenue Larribau, 64018 Pau Cedex, France. galo.sanmiguel@total.com

Abstract

The well exposed outcrops of the upper Kimmeridgian shallow-marine carbonates at Jabaloyas (Iberian Chain, NE Spain) permit the evaluation of geophysical methods for the identification of sedimentary facies. Direct measurement of magnetic susceptibility in facies and detailed grids of magnetometry, electromagnetic multifrequency and ground-penetrating radar (50 to 500 MHz antennas) have been performed in two study areas where the upper Kimmeridgian rocks are nearly horizontal. Magnetometry indicates negative anomalies in residual magnetic field and vertical magnetic gradient related to reef pinnacles and faults. Electromagnetic data reveal that positive anomalies of apparent conductivity correlate with non-reefal facies. The areal distribution of magnetometry and EM data does not permit the unequivocal identification of pinnacles and faults at the studied area. By contrast, ground penetrating radar profiles and maps of relative reflectivity in two way travel time slices are useful for the identification of faults (hyperbolic anomalies) and reefal and non-reefal facies (radar facies A and B, respectively). The integration of geophysical data, mainly ground penetrating radar, has permitted the 3D reconstruction of reef pinnacles and its tectonic framework.

Keywords: Magnetometry, electromagnetic multifrequency, ground-penetrating radar, shallow-marine carbonates, pinnacle reefs, Kimmeridgian, Iberian Chain.

1. Introduction

Limited well data and low resolution of seismic surveys are often the origin of uncertainties at subsurface at different phases in the hydrocarbon field analysis. Modern and ancient sedimentary models facilitate the understanding of sedimentological data, being crucial to better define reservoir heterogeneities (e.g. Asprion and Aigner, 2000; Mancini et al., 2004; Borgomano et al., 2008). These models provide for multi-scale sedimentary heterogeneities that together with diagenetic porosity-enhancing processes can predict the permeability distribution (van Koppen et al., 2015).

The well exposed outcrops of the Upper Jurassic at Jabaloyas in the Sierra de Albarracín (Iberian Chain, NE Spain; Fig. 1a) allow identification of the detailed facies architecture of the upper Kimmeridgian shallow-marine pinnacle reefs and related non-reefal facies which are potential outcrop analogue of carbonate reservoirs in the Middle East and Gulf of Mexico (Mancini et al., 2004; Bádenas and Aurell, 2010; Alnazghah et al., 2013; Pomar et al., 2015; San Miguel et al., 2013). Well exposed outcrop conditions of the Kimmeridgian rocks, especially in the Jabaloyas area, also provide the opportunity for integrated sedimentary and geophysical analyses, including ground-penetrating radar, to evaluate the presence of geophysical contrasts between sedimentological facies.

The application of ground-penetrating radar (GPR) in the characterization of carbonate rocks has been especially focused on tufa deposits (Pedley, 1993; Hill et al., 1998: Brusi et al., 1998; Pedley et al., 2000; Pedley and Hill, 2003, Pedley, 2009; McBride et al., 2012), but also on shallow-marine carbonates (e.g. Pratt and Miall, 1993; Sigurdsson and Overgaard, 1998; Dagallier et al., 2000; Grasmueck and Weger 2002: Asprion et al., 2009; Jorry and Bievre, 2011), some of them including carbonate buildups (Asprion and Aigner 2000; Mukherjee et al., 2012; Nielsen et al. 2004). These works have showed the high resolution of GPR analyses to evaluate the architecture of carbonate rocks, especially for those formed in highly heterogeneous shallow environments where lateral facies changes are usually present. In addition, the combined analysis of GPR analysis and diagenetic and tectonic structures can be suitable for deciphering controls on porosity systems and lateral changes of permeability. Good results have been obtained in the evaluation of carbonate rocks, especially where changes in porosity and internal structure between reefal and related non-reefal facies are present (e.g. Asprion and Aigner, 2000; Mukherjee et al., 2012). GPR quantitative characterization in outcropping sedimentological units is also a future promising field (e.g. Grasmueck et al., 2005; Takayama et al., 2008: Forte et al., 2012).

Due to abrupt lateral facies changes of shallow-water marine carbonates, the high-resolution GPR analysis of these sedimentary bodies requires a detailed grid of survey profiles and a short separation distance between profiles. Detailed surveys are also indispensable when targets are not linear or when their evaluation requires avoiding spatial aliasing (Grasmueck et al., 2005; Forte et al., 2012). Moreover, other geophysical survey techniques can be also evaluated as a tool for the 3D characterization of carbonate facies architecture. In this work different geophysical techniques, including magnetometry, magnetic susceptibility, electromagnetic multifrequency (EM) and ground-penetrating radar (GPR) have been applied to measure magnetic and electromagnetic behaviors of the different facies at the subsurface and in outcrops and selected samples. The surveys have been carried out in a detailed grid of profiles along two sectors: 1) a structural platform exposing a 4 Ha sedimentary surface of reef and non-reefal facies; and 2) along a 200 m-long cliff. The two main objectives have been the 3D geophysical characterization of reefal buildups and related non-reefal facies, and the evaluation of the distribution of faults affecting the studied rocks.

2. Geological and stratigraphic context

The studied upper Kimmeridgian carbonate rocks belong to the Torrecilla Formation cropping out around Jabaloyas in the Sierra de Albarracín (Iberian Chain, NE Spain; Fig. 1a). These rocks originated in the shallow marginal areas of the Iberian basin, on a vast carbonate ramp deepening to the east towards the Tethys Ocean. The sedimentary succession is organized in 5-20 m-thick high-order sequences (Aurell and Bádenas, 2004; Bádenas and Aurell, 2010). Present work concentrates in the thicker high-order sequence (around 20 m) that contains the best outcropping pinnacle reefs (up to 13 m thick and up to 30 m wide), and the widest variety of non-reefal facies (sequence C from Aurell and Bádenas, 2004; Bádenas and Aurell, 2010; San Miguel et al., 2013; Fig. 1b).

From a structural point of view, the studied upper Kimmeridgian rocks were affected by two major tectonic events: an Early Cretaceous rifting stage, with evidences of first pulses during Tithonian times, and a Paleocene compressive event that reactivated previous normal faults and lifted up the area up to 1600 m (e.g., Salas et al., 2001). Around Jabaloyas, the Kimmeridgian rocks are nearly horizontal or dip slightly towards the SE, and NNW-SSE and ENE-WSW sub-vertical normal faults compartmentalize small-size blocks. These blocks tend to form structural platforms of the upper Kimmeridgian sedimentary units where geophysical surveys were carried out.

3. Geophysical survey

3.1. Methodology

A geophysical survey including magnetometry, EM and GPR has been carried out in a structural platform at Puntal de Montero (Figs. 1a and 2a), where pinnacle reefs can be identified in the field and in the aerial photograph. The reefs are presented as circular to elliptical "spots". Moreover, they outcrop in a number of 2D windows on cliffs near Jabaloyas (Barranco de la Canaleja; Fig. 1b), which allow direct observations and geophysical measurements of reefal and non-reefal facies.

Magnetometry has included the measurement of intensity of magnetic field and vertical magnetic gradient in a total of 14.267 points (sensor separation of 0.5 m: Overhauser effect GSM-19 with a plugged GPS). During survey, natural variations of Earth magnetic field were also registered by a second magnetometer. Diurnal correction and residual magnetic anomalies were calculated from both structural platform and cliff datasets. Magnetic susceptibility was measured with a KT-10 device along the outcropping facies in the cliff and at selected hand samples.

EM data at 5 different frequencies (0.5, 5, 18, 35 and 65 KHz) were measured along a grid of parallel profiles on the structural platform, and on profiles over the cliff and close to the cliff edges (18530 points measured). Both surveys were carried out with a GEM-02 device from Geophex. Based on measured data, apparent susceptibility and apparent conductivity were calculated from in-phase and quadrature values (Huang and Won, 2000; Huang, 2005).

GPR analysis was carried out using 50, 100, 250 and 500 MHz antennas with different frequencies (CUI-2 electronic system from Ramac Geosciences with unshielded 50 MHz antennas and 100, 250 and 500 MHz shielded antennas). The 50 MHz survey was repeated changing the polarization array with respect to the displacement including parallel and perpendicular arrays (PL-BD and PR-BD). A preliminary survey evaluated the different antennas to be used in the final survey that in total encompassed around 13 km. Processing consisted in zero time correction, amplitude gain (linear and exponential), out of range frequencies filter and subtract mean trace.

From the direct analysis of GPR profiles, radar facies were defined *sensu* Baker (1991). These correspond to rock bodies characterized by changes in reflectivity, attenuation, internal structure and impedance changes, as well as contacts within and between units. In the case of the high-frequency antennas, net change between the identified radar facies allowed the analysis in TWT (Two Travel Time) slices (see similar approach in Mukherjee et al. 2012). The objective was to evaluate its applicability for the automatic mapping of sedimentological units (e.g. Pueyo Anchuela et al., 2011). The actual depth from TWT intervals was calculated from hyperbolic fitting anomalies (e.g. Reynolds, 1997) with mean values of 9.8 m/μs.

4. Results

4.1. Geophysical survey along the structural platform Puntal de Montero

The studied site at the Puntal de Montero is a platform with homogeneous topography that cut a nearly horizontal sedimentary surface of the upper Kimmeridgian rocks (Fig. 2a). The surveyed area is around 4 Ha. The analysis of the 1/5000 scale aerial photograph permits visual identification at surface of circular to elliptical geometries related to pinnacle reefs ("spots" with more reflectivity in the photographs) and the presence of lineaments that can be interpreted as faults.

Magnetic survey was carried out in 12.388 points along N-S and E-W profiles with a separation below pinnacle dimensions (Fig. 2b). The obtained data of residual magnetic field anomaly showed a low variability of about 4 nT (Fig. 2c). Changes in the vertical magnetic gradient were below 2 nT/m (Fig. 2d). Data map along the surveyed area permitted to identify clusters of higher magnetic field and vertical magnetic gradient but without a clear areal distribution.

EM data at 5 different frequencies (ranging from 0.5 to 65 KHz) were obtained from the N-S oriented profiles (Fig. 3a). They include 18.324 measured points. The calculated apparent magnetic susceptibility shows a homogeneous general trend with the highest contrasts for the most surficial (65 KHz) frequency (Fig. 3b). In the case of the apparent conductivity, changes of this property showed in general very low values and anomalies of some mS/m to some 10´s of mS/m (Fig. 3). Measurements with high frequencies (65 and 18 KHz) showed general low to very low values. Data maps reflect an alignment of peaks with higher values along the central zone of the study area and some local high values in the eastern zone (Fig. 3c, d). At lower frequencies (5 and 0.5 KHz), just isolated peaks of high contrast of apparent conductivity are identified (Fig. 3e, f).

GPR was carried out first in the entire (4 Ha) survey area through mainly E-W oriented profiles using 50, 100, 250 and 500 MHz antennas (Fig. 4). Subsequently, a higher resolution GPR acquisition (250 MHz antenna) was carried out in the zone with higher concentration of pinnacle "spots". Comparison of GPR data obtained with different antennas along the same profile evidences changes in the style of GPR reflectors (Fig. 5a, b) that are more clearly identified at high-frequency antennas (i.e.250 and 500 MHz; Fig. 5c). Areas with a high concentration of hyperbolic anomalies and apparent higher penetration of GPR (radar facies A; Fig. 5a) can be differentiated from areas with lower penetration and higher reflectivity (radar facies B; Fig. 5b). These two facies can be also identified at 100 MHz (Fig. 5d), but are not evident at 50 MHz (Fig. 5e). Reflectors of radar facies A are usually heterogeneous in comparison with the clear reflector definition of radar facies B (Fig. 5b). At shallow subsurface, areas of radar facies B have concave-plane geometries, adapting with on-lap geometries to the areas of radar facies A; in other cases the boundary between these radar facies is sharp. In detail, meter-scale hyperbolic anomalies have been also identified at higher depths, more clearly at high frequency profiles. These anomalies include isolated anomalies with symmetrical and asymmetrical branches (see Fig. 5c).

A geophysical profile of the stratigraphic platform has been selected to evaluate the correlation of magnetic and electromagnetic data with aerial photograph and field data (Fig. 6). The direct comparison is not univocal, although a subtle correlation between apparent conductivity peaks, magnetic dipoles and changes in radar facies can be identified. By contrast, GPR and field data show a more clear correlation, as radar facies A is usually coincident with reefal facies in the field, and radar facies B with non-reefal facies. Hyperbolic anomalies at middle depths or net interruptions of the lateral continuity of reflectors at shallow conditions are considered to be related to faults, being some of them identifiable in the aerial photograph.

4.2. Geophysical survey along the cliff: Barranco de la Canaleja

The cliff at Barranco de la Canaleja, close to Jabaloyas village, has been analyzed in order to directly compare the different sedimentological facies together with magnetic and electromagnetic data measured in the field (Fig. 7).

Magnetic susceptibility has been measured directly on the different facies in outcrops and hand samples (229 measured points; Fig. 7a). Data show low values and overlapping distribution, with values from reefal facies ranging between -2 to 6 x 10^{-6} SI, whereas non-reefal facies have higher values between 3 and 10 x 10^{-6} SI. The highest identified values correspond to mud-supported non-reefal facies.

In spite of these low contrasts, the magnetometry survey on top of the cliff and cliff edges (1879 points in total) reflects some anomalies of Earth magnetic field that seems to be related to the volumetric contribution of each facies in the vertical profile (Fig. 7b). Lower values of residual magnetic field are found in areas with highest contribution of reefal facies, whereas values systematically increase, in the range of 2- 4 nT, in areas with higher contribution of non-reefal facies. The combination of field and magnetometry data permits to identify the relationship between facies changes and distribution of magnetic anomalies; however, non univocal interpretations can be done from the magnetic data without field information. By contrast, the vertical magnetic gradient, which is more sensitive than the intensity of the magnetic field, permits to identify anomalies at the contacts between reefal and non-reefal facies (Fig. 7b).

Similarly, EM results with different frequencies have been compared with the outcropping units in the cliff (Fig. 8a). Obtained data of apparent conductivity show subhorizontal trends or changes that do not correlate with facies changes. Only 1.5 KHz data define 3 net anomalous peaks of high values, which correspond to non-reefal facies (Fig. 8a). The apparent susceptibility values show homogeneous trends (except for the 18 KHz frequency that shows high values in the central zone), but without correlation with sedimentological facies changes. In order to evaluate more directly the distribution of apparent conductivity changes and facies, a tomography of apparent conductivity was done (Fig. 8b). Although there is not a point- to- point correlation with the identified facies, a general decrease of apparent conductivity is observed in sectors including reefal facies and, conversely, a progressive or sudden increase of the apparent conductivity correlates with non-reefal facies.

5. Discussion

5.1. EM and magnetometry data

In the studied structural platform, the independent evaluation of magnetometry and EM data maps has no clear usefulness to characterize the distribution of pinnacle reefs and related non-reefal facies in subsurface. In the cliff, there are some relationships of geophysical data with sedimentological facies (i.e., positive anomalies in magnetic field and apparent conductivity related to non-reefal facies; anomalies in the vertical magnetic gradient recorded at the contacts between reefal and non-reefal facies), but without enough contrast to permit their univocal interpretation.

Magnetometry and EM data obtained in the detailed studied zone at the structural platform have been compared and contrasted with the mapping of pinnacle “spots” and fault traces obtained from field and aerial photograph data (Fig. 9a, b). This comparison reveals that, as a general rule, reefal facies coincide with relative lower values of magnetic field and vertical magnetic gradient, whereas non-reefal facies correlate with positive anomalies, although these anomalies do not exactly fit with the pinnacle geometry in the subsurface. It is noteworthy that positive anomalies in magnetic field also relate to non-reefal facies in the cliff (see Figs. 7 and 8) and high values of magnetic susceptibility has been measured directly in mud-supported non-reefal facies. These results are coherent with measured susceptibility and earth magnetic field values and they can be interpreted in terms of presence of higher matrix mud proportions within the non reefal facies. In addition, distribution of magnetic anomalies (lineaments of dipoles), especially in vertical gradient, correlates with the identified fault traces. In other cases, these anomalies are parallel but not exactly coincident with the identified faults traces.

Concerning EM results, the apparent susceptibility values show very low changes and do not define any geometry potentially correlatable with pinnacles in the underground (see Figs. 8 and 9). However, the apparent conductivity with intermediate frequencies reveals areas of high values that correlates with non-reefal facies, specially where the identified faults in the field are superimposed (Fig. 9e, f). This is coherent with data obtained in the cliff, where peaks of high values of apparent conductivity were identified in the profiles and in the tomography (see Fig. 8b).

In summary, negative anomalies in the Earth magnetic field, vertical gradient and apparent conductivity relate in general to pinnacles at the subsurface. However, magnetometry and EM data without direct field observations are not enough for the interpretation of facies distribution (Table 1). In spite of this, these techniques could be systematically performed for selecting sectors where detailed GPR analysis can be performed.

5.2. GPR data

GPR data reflect clear different reflector patterns for pinnacle reefs (radar facies A) and non-reefal facies (radar facies B). Changes in geometry and style of different radar facies of reefal and non-reefal facies have been also documented by Asprion and Aigner (2000).

Reefal buildups have been identified as radar facies with abundant reflections dominated by overlapping of hyperbolas (Sigurdsson and Overgaard, 1998). Even reflectivity changes have been used to evaluate the distribution of reefal facies (Mukherjee et al., 2012). In all these cases, an increase of penetration of GPR was identified for reefal facies against non-reefal facies.

Similar conclusions can be inferred from the GPR data obtained in this case study, regarding radar facies, penetration depth and distribution. GPR has resulted as a valuable tool for the identification of the two main reefal and non-reefal facies, in particular with 500 and 250 MHz antennas (see Fig. 5), and where the reefs are nearly exposed. In addition, data from the detailed studied zone in the structural platform (see Fig. 9a, b) reveal that GPR can be useful for the 2.5D evaluation of facies. GPR profiles obtained with 250 MHz antennas (Fig. 10) show a clear differentiation between high concentration of anomalies and high apparent penetration (radar facies A: pinnacle reefs) and areas with homogeneous and reflective media with minor penetration (radar facies B: non-reefal facies). These changes have been followed both along different parallel profiles (Fig. 10a), but also along transversal directions (Fig. 10b). GPR data from 250 MHz or 500 MHz also reflect a general net contact between both radar facies at middle depths; and on-lap geometries of radar facies B (non-reefal facies) over radar facies A (reefal facies) at shallow depths. These data are coherent with the net or on-lap sedimentary contacts between reefal and non-reefal facies and local fault contacts observed in the field (Fig. 1b). Different penetration of each radar facies and reflective variations between them allow the quantitative evaluation of relative reflectivity in terms of TWT slices (e.g. Mukherjee et al., 2012). The analysis of the relative reflectivity through time slices has been performed for the 250 MHz profiles of the detailed studied zone of the structural platform (Fig. 11a). Based on the different penetration of reflectors of each radar facies, high relative reflectivity at shallow TWT slices would be related to non-reefal facies, whereas at higher depths, positive anomalies of relative reflectivity indicate reefal facies due to the high attenuation of reflectors at non-reefal facies. Lastly, obtained results of the relative reflectivity through TWT slices with the 250 MHz devices and comparison with the aerial photograph (Fig. 11c) confirm these predictions. In particular: 1) for time intervals shallower than 1 m, pinnacles do not show distinctive signatures in the slice or they correspond to negative anomalies of relative reflectivity. Positive anomalies surround some of the identified pinnacles, especially in sectors where non horizontal and accommodated reflectors of radar facies B are identified; 2) at greater depths (e.g. $z>1.7$ m), groups of circular positive anomalies are identified and correlate with pinnacles. Boundaries of these circular anomalies are defined by high gradients in reflectivity change, which locally can involve more than one isolated anomaly; and 3) in some cases, the limits of the positive anomalies present rectilinear margins, which almost correlate with mapped faults without significant vertical movement (Table 1). However, these faults do not produce significant reflectivity anomalies and their identification is more evident when they bound both radar facies. Otherwise, where there is not a net change in reflectivity, the faults are identified by the anisotropy of the external envelopes of reflectivity changes or their nearly rectilinear shape (Fig. 11c).

5.3. Integrated 2.5D data model

GPR data show a clear distinction of radar facies A (corresponding to sedimentological reefal facies) and B (non-reefal facies). However their distribution and lateral contacts can be only achieved at the high-frequency profiles that have enough resolution only at shallow depths (up to 7-8 m depth; see Fig. 5). This limited penetration excludes the possibility to study the complete pinnacle thickness, which is expected to be up to 13 m (see Fig. 1b). In another hand, the use of low-frequency antennas that reach higher depths does not permit a clear discrimination of both radar facies (see Fig. 5). These problems in data resolution can be avoided by comparing low- and high-frequency profiles. For example, the compared analysis of

50 MHz and 250 MHz profiles (Fig. 12a) allows identifying sharp contacts between radar facies at the high-frequency devices that can be prolonged in depth at the low-frequency profiles.

The correlation between high-frequency and low-frequency profiles has permitted to create a 2.5D data model of pinnacle distribution (radar facies A) for the studied zone (Fig 12b). The model has been carried out identifying the radar facies in shallow subsurface, i.e. in high-frequency profiles, and prolonging their contacts in depth through the low-frequency profiles. Reached depth of the survey was not clearly identified as a reflector, being observed a general attenuation and progressive loose of resolution with depth. The lower contact in the model has been considered as the average actual reached depth of the studied profiles. The lateral distribution of radar facies and the interpretation of their prolongation in depth have permitted to obtain a 2.5 model to evaluate the distribution of pinnacles and faults in a 3D fashion. In field view the pinnacles appear as isolated buildups, but the model indicates they can also be coalescent forming “ribbons” of pinnacles. This agrees with data obtained by direct measurements of 89 pinnacle reefs around the Jabaloyas area (San Miguel et al., 2013). Pinnacles tends to grow more vertically than laterally in distal domains, with height/width ratios close to 1 and higher density towards proximal areas, where can form 50 m-long “ribbons” in proximal domains. The identification of this kind of distribution allows not only a better definition of the pinnacle morphology in the studied zone, but also to understand the 3D facies changes at isolated outcrop windows of such kind of units.

6. Conclusions

Integrated geophysical analyses and calibration of data with direct outcrop measurements has been carried out at the upper Kimmeridgian shallow-water pinnacle reefs and related non-reefal facies at Jabaloyas (NE Spain). These results have allowed evaluating the usefulness of these techniques for the identification of reef pinnacles and faults in the shallow subsurface. Moreover these data defines the interest of integration of magnetometry, EM and GPR analysis to improve knowledge of the sedimentological heterogeneities and their 3D distribution.

Magnetometry and EM results indicate negative anomalies in the Earth magnetic field or vertical magnetic gradient and apparent conductivity negative anomalies over the reef pinnacles. In addition, direct measurements of magnetic susceptibility reveal lower values for these reefal facies. However, the contrast of magnetometry and EM data between reefal and non-reefal facies is not enough to permit the univocal interpretation of the facies distribution in the subsurface. In spite of that, these techniques can be used to select areas for later detailed GPR analysis, as similar shallow-water successions without pinnacle reefs should show relative homogeneous magnetic and electromagnetic behaviors.

GPR survey has allowed identifying two main radar facies A and B that correspond to reefal and non-reefal facies, respectively. Integrated evaluation of field and GPR data has permitted to obtain maps of the reef distribution through direct analysis of GPR profiles and through relative reflectivity changes in TWT slices. Both approaches have allowed evaluating the applicability of GPR for the characterization of facies changes at shallow subsurface, but also to correlate these changes along deeper intervals in low-resolution profiles. In addition, these data have permitted to create a 2.5D model that defines the morphology and the lateral extension of pinnacles and the location and distribution of fractures affecting the studied stratigraphic interval.

Acknowledgements

This research has been supported by Research Groups of Zaragoza University H54 (Reconstrucciones Paleoambientales; IUCA) and E27 (Geotransfer) supported by Aragón Government and FEDER founds, and project CGL2014-53548 (Spanish Ministry of Science and

Innovation). Authors want to acknowledge comments and suggestions from Alex MacNeil, associate editor, and three anonymous reviewers.

Figure and table captions

Figure 1. (a) Geological map and location of the upper Kimmeridgian rocks in the two studied sectors, Barranco de la Canaleja and Puntal del Montero, close to Jabaloyas (Teruel province, NE Spain) A simplified log of the geological series from the studied zone is included. (b) Overview of the reef pinnacles and related non-reefal facies in the cliff of Barranco de la Canaleja close to Jabaloyas. These facies belongs to a deepening-shallowing high-order sequence (sequence C in Aurell and Bádenas, 2004; Bádenas and Aurell, 2010; San Miguel et al., 2013). Inset a detail from the facies changes in the upper part of the reefs is included.

Figure 2. Magnetometry data in the structural platform at Puntal del Montero. (a) Aerial photograph of the structural platform. Faults (see straight lineaments) and pinnacle reefs (see “spots” with high reflectivity) can be identified (see cartography in figure 8b). (b) Location of N-S and E-W oriented profiles of the magnetic survey, which encompass a total of 12388 measured points (c, d) Maps of the obtained data of residual magnetic anomaly and vertical magnetic gradient, respectively.

Figure 3. EM data in the structural platform at Puntal del Montero. (a) Location of EM profiles, which encompass a total of 18324 measured points. (b) Map of apparent susceptibility obtained for the measurement at 65 KHz frequency. (c, d, e, f) Maps of apparent conductivity with 65 to 0.5 KHz antennas.

Figure 4. Location of the GPR survey at the structural platform in Puntal de Montero, with 500 MHz antenna (2 profiles, see blue arrow), 100 and 200 MHz antennas (14 profiles each, see yellow arrows) and 50 MHz antenna in the detailed studied zone (56 profiles in total). GPR results are included in figures 5 and 10.

Figure 5. Compared analysis of GPR results obtained at the structural platform in Puntal del Montero for the same profile with different central frequencies antennas. (a) Location of the analyzed profile (see red arrow). (b) Detail of the 250 MHz profile (see red box in c) indicating the two identified radar facies A and B. (c, d, e) GPR data obtained from different antennas. Note that different depths have been analyzed for each antenna. In figure c, isolated asymmetric and symmetric anomalies are also indicated. In figure e, 50 MHz profiles include different orientation of antennas during survey (PL-BD and PR-BD). Note radar facies A and B are not evident at 50 MHz.

Figure 6. Compared analysis for the most representative geophysical data obtained at the structural platform in Puntal de Montero in a selected profile (see black line in the aerial photograph). Radar facies A and B identified in the GPR profile are also indicated. Note there is not a clear correlation of magnetometry and EM data with GPR and field data. However, GPR and field data can be correlated: radar facies A corresponds to pinnacle reefs and radar facies B correlates with non-reefal facies. Hyperbolic anomalies at middle depths or net interruptions of the lateral continuity of reflectors at shallow conditions are considered as related to faults.

Figure 7. Magnetometry and EM data obtained in the cliff of Barranco de la Canaleja close to Jabaloyas. (a) Plot of the apparent susceptibility data for reefal and non-reefal facies measured at outcrop and hand samples (see detailed distribution of facies in figure 1b). Highest values of apparent susceptibility correspond to mud-supported non-reefal facies. (b) Photograph from the Barranco de la Canaleja cliff and distribution of magnetometry data (residual magnetic anomaly and vertical magnetic gradient). Two different profiles are included in order to evaluate data variation, anomalies and data trends along the same transect over the cliff (see green and purple lines). Potential noisy areas are also indicated.

Figure 8. (a) EM data (apparent conductivity and apparent susceptibility) and (b) tomography of apparent conductivity along the same transect for different analyzed frequencies. The yellow line in the field image corresponds to 1.5 KHz frequency.

Figure 9. Comparison of field, aerial photograph data, magnetometry and EM data in the detailed studied zone of the structural platform at Puntal del Montero. (a, b) Location of the detailed studied zone (see black box in a) and mapping of pinnacle reefs and faults. (c, d, e, f) Magnetometry data (residual magnetic field and vertical magnetic gradient) and EM data (apparent conductivity for 18 KHz and 0.5 KHz). The cartography of faults and pinnacles is superimposed for comparison.

Figure 10. GPR profiles with 250 MHz antennas along the detailed studied zone of the structural platform (see location in figure 9a). (a) E-W parallel profiles indicating the two defined radar facies. Note the sudden and subvertical contact between both radar facies. (b) In the N-S profile, shallow reflectors of radar facies B are tilted to the S.

Figure 11. Analysis of relative reflectivity in TWT slices along the detailed studied zone of the structural platform (see location in figure 9a). a) Aerial photograph from the detailed studied zone and mapping of pinnacle reefs and faults. In the aerial photograph, processing has been applied to highlight the identified areas with higher reflectivity (pinnacle reefs). (b) Example of identified radar facies along a high-frequency profile for comparison with their electromagnetic characteristics in different TWT slices (z= depth). (c) Relative reflectivity for different TWT slices. The location of the deepest slice (i.e. slice 6) is indicated with a blue line in figure b. The location of the profile and the cartography of faults and pinnacles is also indicated.

Figure 12. Model of distribution of pinnacles and faults in the studied zone based on the integrated GPR data in the detailed studied zone of the structural platform. (a) Compared analysis of two selected 50 and 250 MHz GPR profiles. Note that the discrimination between

radar facies A (pinnacle reefs) and B (non-reefal facies) can be easily performed in the 250 MHz profile, but not in the 50 MHz profile. However the sharp contacts between radar facies in the 250 MHz profile can be prolonged in the 50 MHz profile. Considering this correlation, the reached depth of GPR survey can be increased integrating both groups of profiles. (b) Model of distribution of pinnacles and faults based on the integration of 50 and 250 MHz profiles. In some cases, pinnacles show straight contacts that correspond to faults, seen in the aerial photograph or indentified in the GPR profiles as hyperbolic anomalies. The grey area at the bottom indicates the mean reached depth of the GPR survey (around 11 m).

Table 1. Summary of the geophysical data obtained in the upper Kimmeridgian at Jabaloyas and their applicability for identification of facies and faults at shallow subsurface.

References

Alnazghah, M.H., Bádenas, B., Pomar, L., Aurell, M., Morsilli, M., 2013. Facies heterogeneity at interwell-scale in a carbonate ramp, Upper Jurassic, NE Spain. Mar. Petrol. Geol, 44, 140–163.

Asprion, U., Aigner, T., 2000. An initial attempt to carbonate buildups using ground-penetrating radar: an example from the Upper Jurassic of SW-Germany. Facies 42, 245–252.

Asprion, U., Westphal, H., Niemanm M., Pomar, L., 2009. Extrapolation of depositional geometries of the Menorcan Miocene carbonate ramp with ground-penetrating radar. Facies 55, 37–46.

Aurell, M., Bádenas, B., 2004. Facies and depositional sequence evolution controlled by high-frequency sea-level changes in a shallow-water carbonate ramp (late Kimmeridgian, NE Spain). Geol. Mag. 141, 717–733.

Bádenas, B., Aurell, M., 2010. Facies models of a shallow-water carbonate ramp based on distribution of non-skeletal grains (Kimmeridgian, Spain). Facies 56, 89–110.

Baker, P.L., 1991. Response of ground penetrating radar to bounding surfaces and lithofacies variations in sand barrier sequences. Expl. Geophys. 22, 19–22.

Borgomano, J.R.F., Fournier, F., Viseur, S., Rijkels, L., 2008. Stratigraphic well correlations for 3-D static modeling of carbonate reservoirs. AAPG Bulletin 92, 789–824.

Brusi, D., Palli, L., Roque, C., Capella, I., Pujadas, A. Vehi, M., 1998. Geophysical electromagnetic prospection in the spatial location of the travertine deposits of the Banyoles depression (Girona). Geological and hydrological implications. Proc. Environ. Eng. Geophys. Soc. Vol. 1, 205–208.

Dagallier, G., Laitinen, A., Malartre, F., Van Campenhout, I. P.A.M., Veeken, P. C.H., 2000. Ground penetrating radar application in a shallow marine oxfordian limestone sequence located on the eastern flank of the Paris Basin, NE France. Sediment. Geol. 130, 149–165.

Forte, E., Pipan, M., Casabianca, D., Di Cuia, R., Riva, A., 2012. Imaging and characterization of a carbonate hydrocarbon reservoir analogue using GPR attributes. Journal of Applied Geophysics 81, 76–87.

Grasmueck M, Weger R., 2002. 3D GPR reveals complex internal structure of Pleistocene oolitic sandbar. Leading Edge of Exploration, Society of Exploration Geophysics 21 (7), 634–639.

Grasmueck, M., Viggiano, D., Smith, L., Nyahay, R., 2005. 3-D vision Ground Penetrating Radar (GPR): Reservoir anatomy beyond the outcrop surface. AAPG Annual Meeting, AAPG Search and Discovery Article #90039.

Hill, I., Pedley, H.M., Denton, P., 1998. GPR, GPS and Promax, applied to the detailed sedimentary architecture of tufa deposits. Proc. Environ. Eng. Geophys. Soc. Vol 1. , 433–437.

Huang, H., 2005. Depth of investigation for small broadband electromagnetic sensors. Geophysics 70 (6), 135–142.

Huang, H., Won, J.J., 2000. Conductivity and susceptibility mapping using broadband electromagnetic sensors. J.Environ. Eng. Geophys. 5, 31–41.

Jorry, S.J., Biévrem G., 2011. Integration of Sedimentology and ground-penetrating radar for high-resolution imaging of a carbonate platform. Sedimentology 58, 1370–1390.

Mancini, E., Llinás, J.C., Parcell, W.C., Aurell, M., Bádenas, B., Leinfelder, R.,Benson, J., 2004. Upper Jurassic Thrombolite Reservoir Play, Northeastern Gulf of Mexico. AAPG Bulletin 88, 1573–1602.

Mukherjee, D., Khan, S.D., Sullivan C., 2012. Upper Albian rudist buildups of the Edwards Formation in central Texas: A GPR- assisted reservoir analog study. Sediment. Geol. 247-248, 71–81.

McBride, J.H., Guthrie, W.S., Faust D.L., Nelson S.T., 2012. A structural study of thermal tufas using ground-penetrating radar. J. Appl. Geophys.81, 38–47.

Nielsen, L., Boldreel, L.O., Surlyk, F., 2004. Ground-penetrating radar imaging of carbonate mound structures and implications for interpretation of marine seismic data. AAPG Bulletin 88, 1069–1082.

Pedley, H.M., 1993. Sedimentology of the Late Quaternary tufas in the Wye and Lathkill valleys, North Derbyshire. Proc. Yorks. Geol. Soc. 49, 197–206.

Pedley, M., 2009. Tufas and travertines of the Mediterranean region: a testing ground for freshwater carbonate concepts and developments. Sedimentology 56, 221–246.

Pedley, M., Hill, I., 2003. The recognition of barrage and paludal tufa systems by GPR: case studies in the geometry and correlation of Quaternary freshwater carbonates. In: Bristow, C.S., Jol, H.M. (Eds.), Ground penetrating radar in sediments: Geological Society, London, Special Publication 211, pp. 207–223.

Pedley, H.M., Hill, I., Denton, P., Brasington, J., 2000. Three dimensional modeling of a Holocene tufa system in the Lathkill Valley, north Derbyshire, using ground penetrating radar. Sedimentology 47, 721–737.

Pomar L., Aurell M., Bádenas B., Morsilli M., Al-Awwad, S.F., 2015. Depositional model for a prograding oolitic wedge, Upper Jurassic, Iberian basin. *Mar. Petrol. Geol.*67, 556–582.

Pratt, B.R., Miall, A.D., 1993, Anatomy of a bioclastic grainstone megashoal (Middle Silurian, southern Ontario) revealed by ground-penetrating radar. Geology 21, 223–226.

Pueyo Anchuela, Ó., Casas-Sainz, A.M., Pocoví Juan, A., Soriano, M.A., 2011. Applying GPR-amplitude wave maps and Am-scans as a semi-quantitative approach to the internal structure of sediments. J. Appl. Geophys. 75: 151–160.

Reynolds, J.M., 1997. An introduction to applied and environmental geophysics. Wiley, Chichester, 806 pages.

Salas, R., Guimerà, J., Más, R., Martín-Closas, C., Meléndez, A., Alonso, A., 2001. Evolution of the Mesozoic central Iberian Rift System and its Cainozoic inversion (Iberian Chain). Mémoires du Muséum Nationale de l'Histoire Naturelle 186, 145–85.

San Miguel, G., Aurell, M., Bádenas, B., Martínez, V., Caline, B., Pabian-Goyheneche, C., Rolando, J., Grasseau, N., 2013. Facies heterogeneity of a Kimmeridgian Carbonate Ramp (Jabaloyas, eastern Spain): a combined outcrop and 3D geomodelling analysis. Journal of Iberian Geology, 39, 233–252.

Sigurdsson, T., Overgaard, T., 1998. Application of GPR for 3-D visualization of geological and structural variation in a limestone formation. J. Appl. Geophys. 40: 29–36.

Takayama, P., Menezes, P., Travassos, J., 2008. High-Resolution 3D GPR imaging of carbonate analogue reservoirs. Proceedings of 33rd International Geological Congress, 234–237.

van Koppen, J.K.J., Al-Menhali, H., Alblooshi, A., Caline, B., Guy, L., Kheidri, H., Hu, T., Kwasniewski, A., Dubois, L., San Miguel, G., Duval, C., Deviese, E., Thomas, E., Vanhalst, M., Dreno, C., and Mel, R., Elhami, M., 2015. Geological Mapping of early Diagenetic Bodies as a Tool to Distribute Permeability in a Mature Giant Carbonate Field. ADIPEC Conference. Technical programme Abstracts.

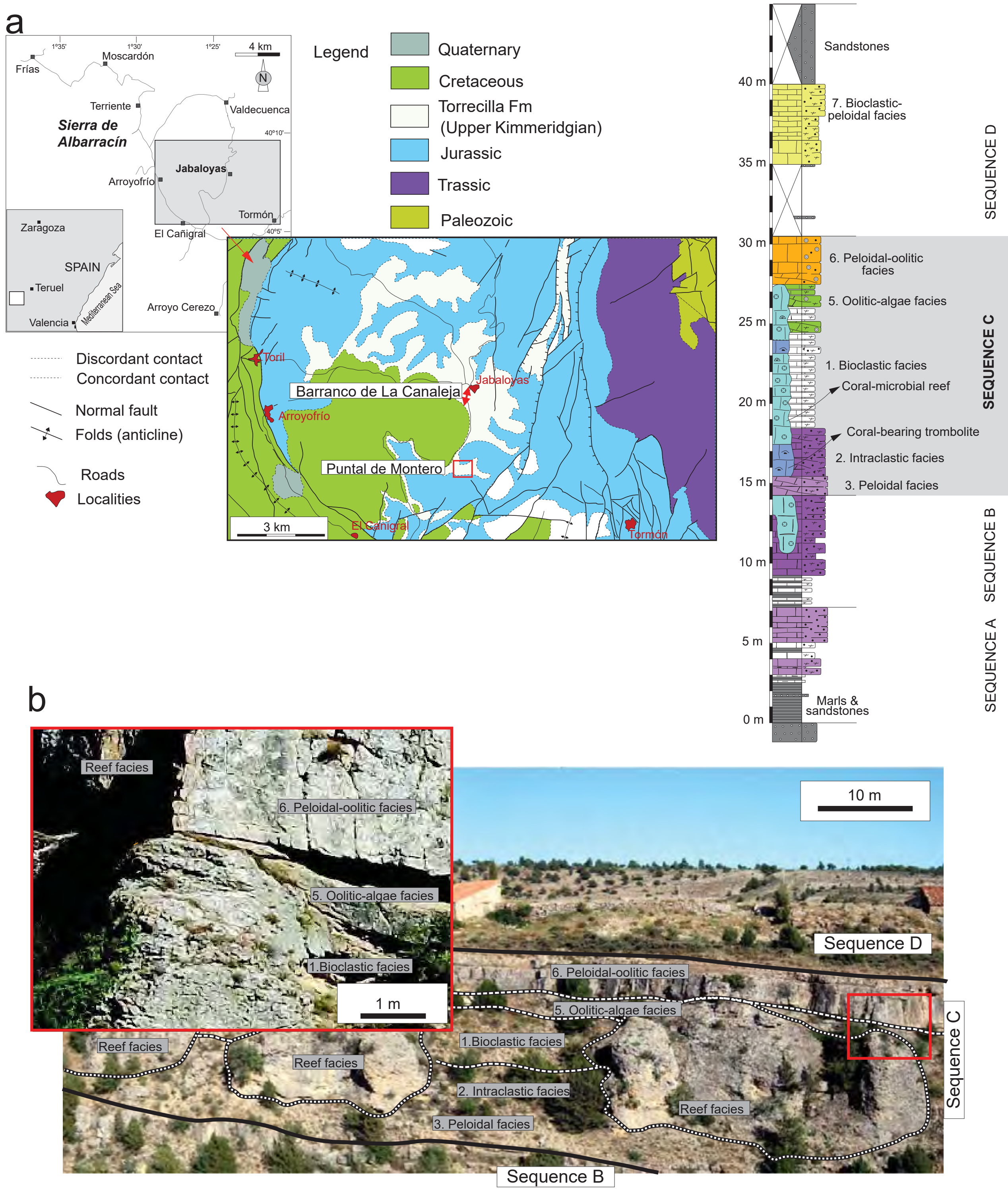
a
Legend
Quaternary
Cretaceous
Torrecilla Fm
(Upper Kimmeridgian)
Jurassic
Trassic
Paleozoic
Frías
Moscardón
Terriente
Valdecuenca
Sierra de
Albarracín
Jabaloyas
Arroyofrío
Tormón
El Cañigral
Arroyo Cerezo
Zaragoza
SPAIN
Teruel
Valencia
Mediterranean Sea
4 km
N
Discordant contact
Concordant contact
Normal fault
Folds (anticline)
Roads
Localities
Toril
Barranco de La Canaleja
Jabaloyas
Arroyofrío
Puntal de Montero
3 km
El Cañigral
Tormón
Sandstones
40 m
7. Bioclastic-
peloidal facies
35 m
SEQUENCE D
30 m
6. Peloidal-oolitic
facies
5. Oolitic-algae facies
25 m
1. Bioclastic facies
Coral-microbial reef
20 m
SEQUENCE C
Coral-bearing trombolite
2. Intraclastic facies
15 m
3. Peloidal facies
10 m
SEQUENCE B
5 m
SEQUENCE A
Marls &
sandstones
0 m
b
Reef facies
6. Peloidal-oolitic facies
5. Oolitic-algae facies
1.Bioclastic facies
1 m
10 m
Sequence D
6. Peloidal-oolitic facies
5. Oolitic-algae facies
1.Bioclastic facies
Reef facies
Reef facies
2. Intraclastic facies
3. Peloidal facies
Reef facies
Sequence C
Sequence B

Figure 1

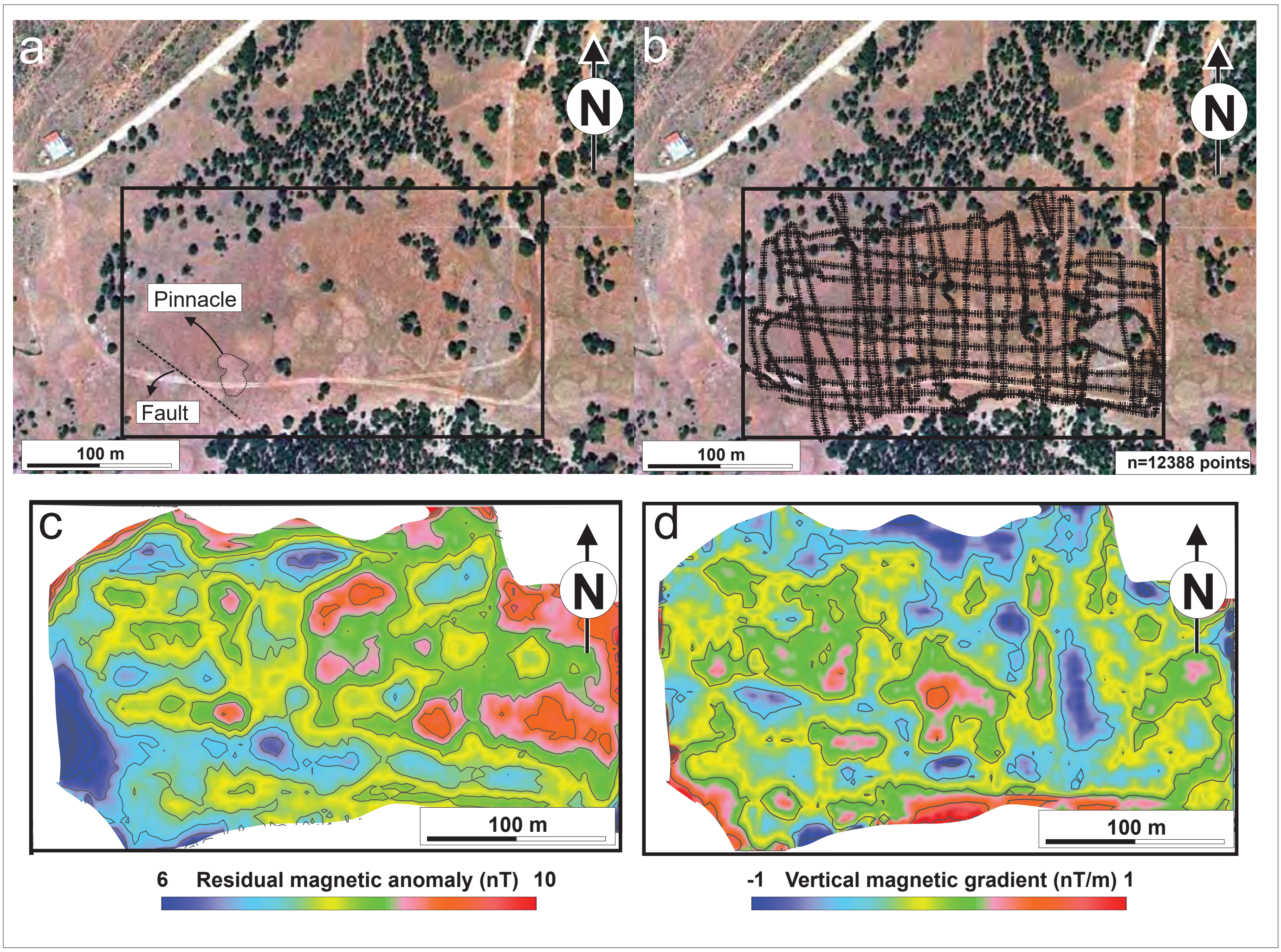
a
b
N
Pinnacle
Fault
100 m
n=12388 points
c
d
6 Residual magnetic anomaly (nT) 10
-1 Vertical magnetic gradient (nT/m) 1

Figure 2

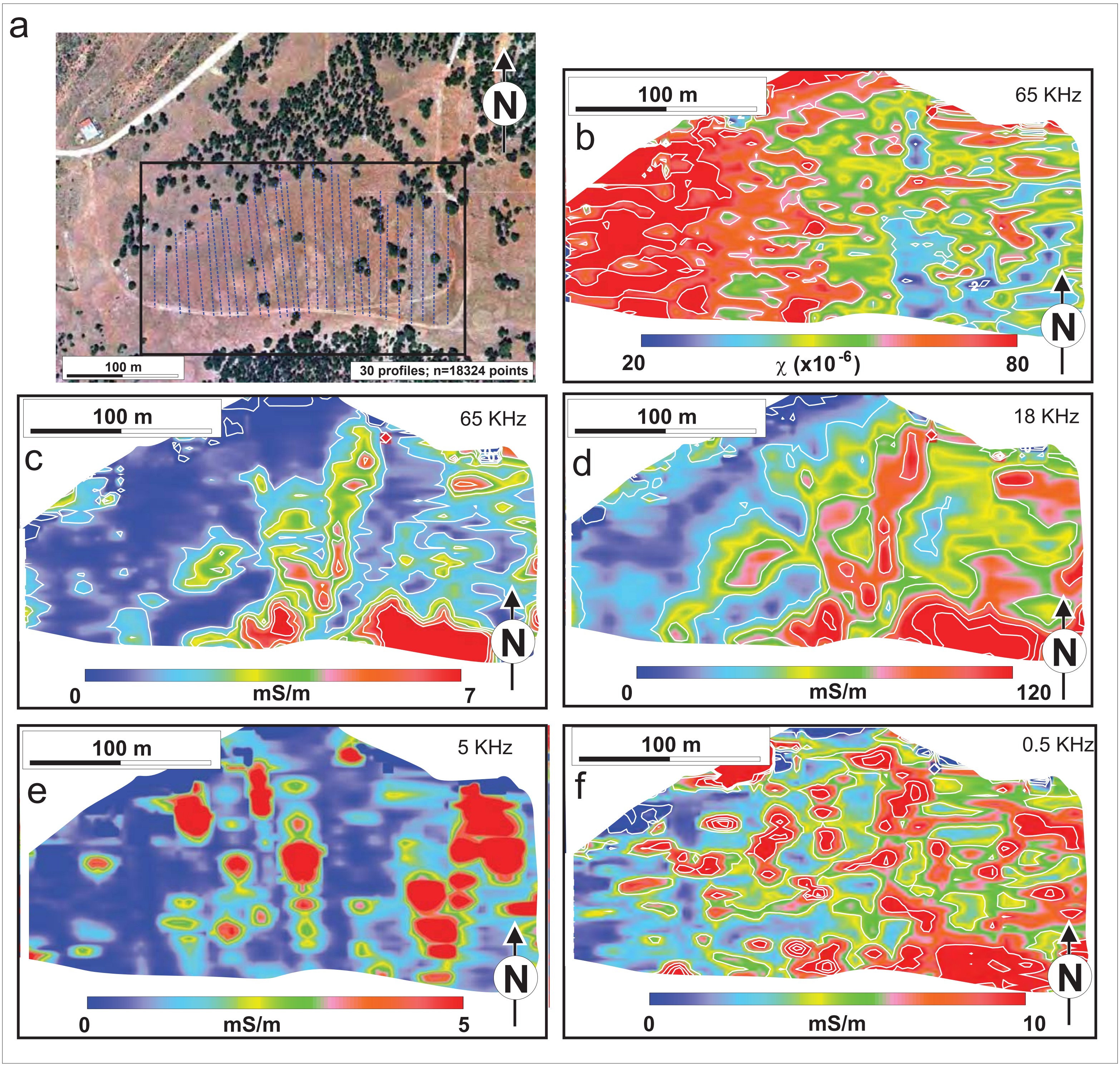
a
N
100 m
30 profiles; n=18324 points
b
100 m
65 KHz
20
χ (x10^-6)
80
c
100 m
65 KHz
0
mS/m
7
d
100 m
18 KHz
0
mS/m
120
e
100 m
5 KHz
0
mS/m
5
f
100 m
0.5 KHz
0
mS/m
10

Figure 3

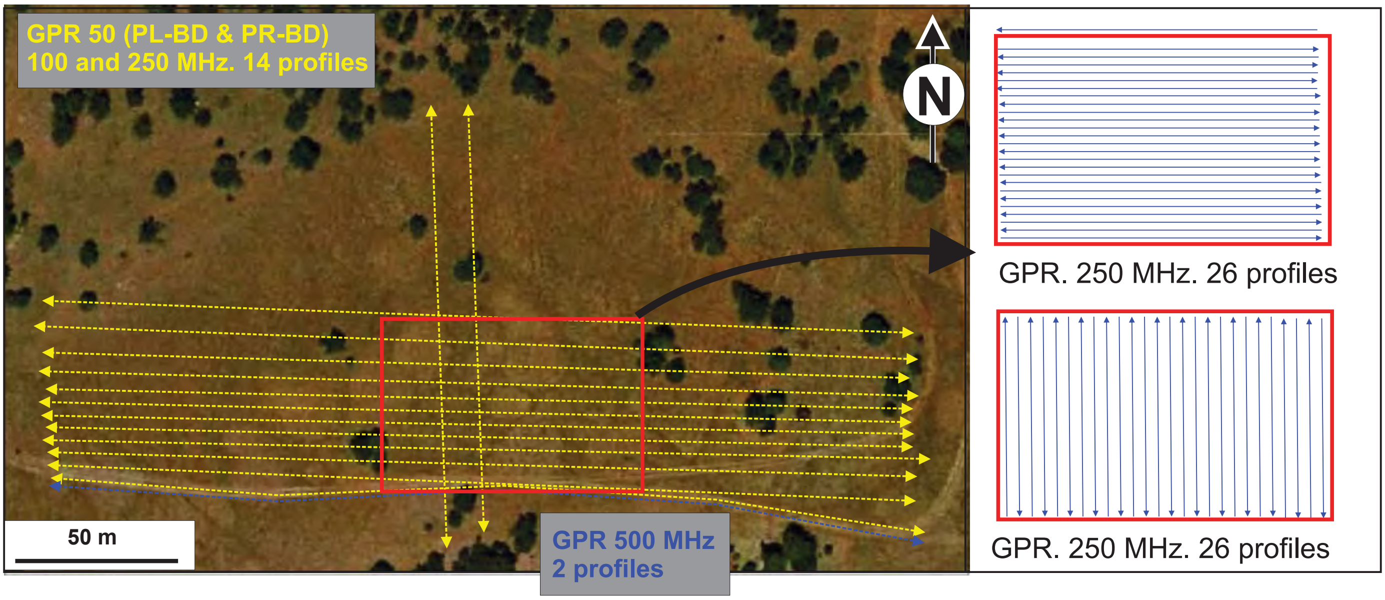
GPR 50 (PL-BD & PR-BD)
100 and 250 MHz. 14 profiles
N
50 m
GPR 500 MHz
2 profiles
GPR. 250 MHz. 26 profiles
GPR. 250 MHz. 26 profiles

Figure 4

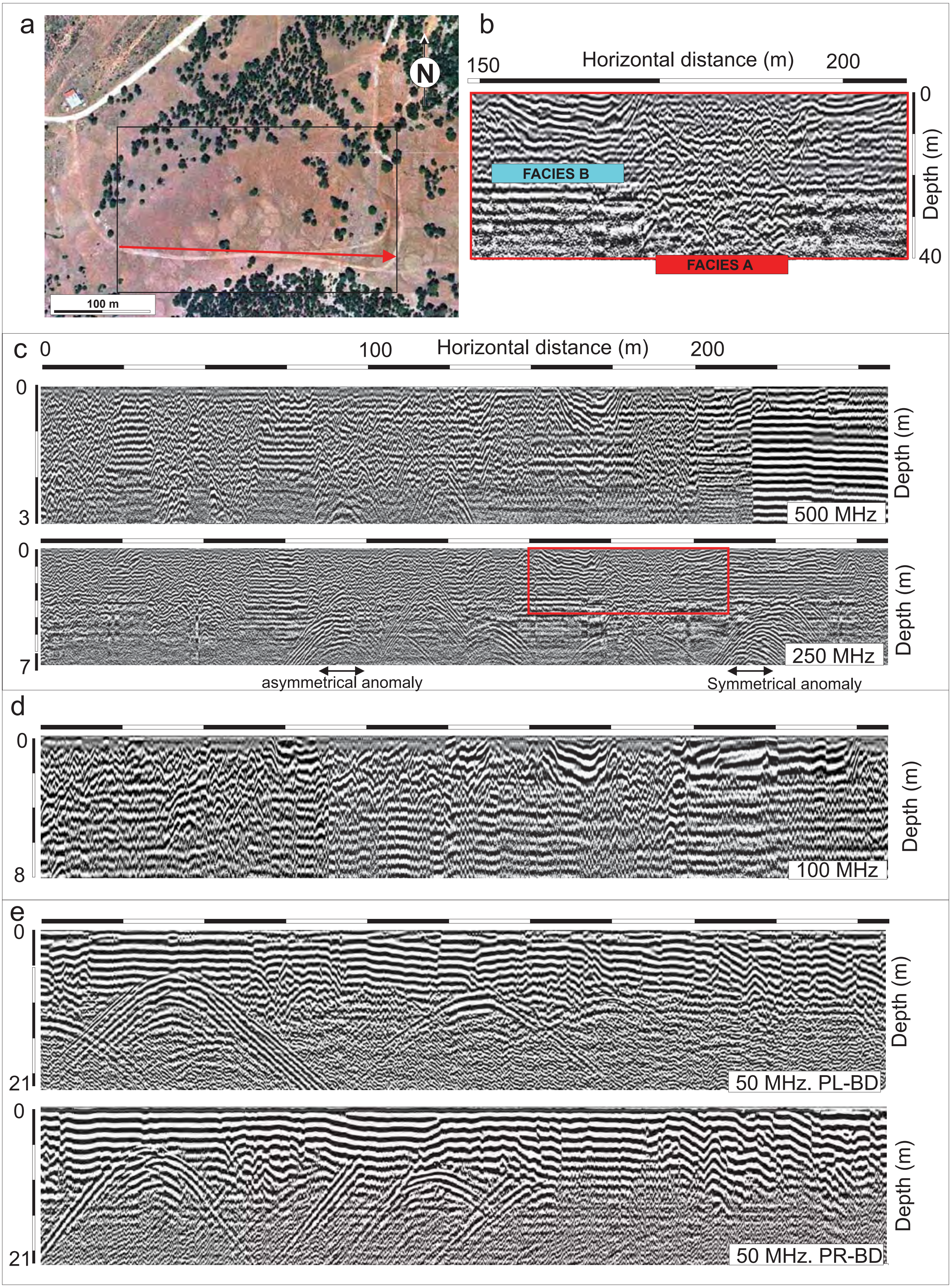

a
N
100 m
b
150
Horizontal distance (m)
200
0
Depth (m)
40
FACIES B
FACIES A
c
0
100
Horizontal distance (m)
200
0
3
Depth (m)
500 MHz
0
7
Depth (m)
250 MHz
asymmetrical anomaly
Symmetrical anomaly
d
0
8
Depth (m)
100 MHz
e
0
21
Depth (m)
50 MHz. PL-BD
0
21
Depth (m)
50 MHz. PR-BD

Figure 5

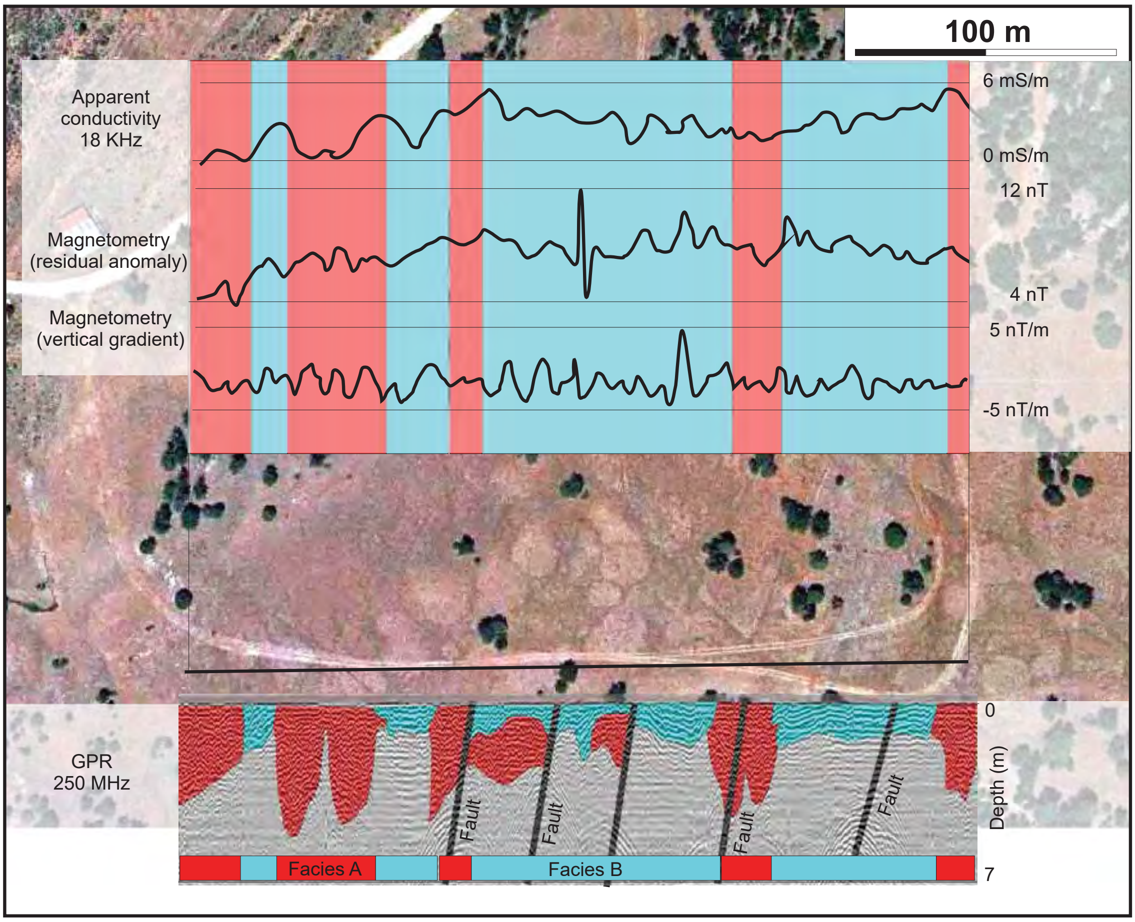
100 m
Apparent conductivity 18 KHz
6 mS/m
0 mS/m
12 nT
Magnetometry (residual anomaly)
4 nT
Magnetometry (vertical gradient)
5 nT/m
-5 nT/m
GPR 250 MHz
0
Depth (m)
7
Fault
Fault
Fault
Fault
Facies A
Facies B

Figure 6

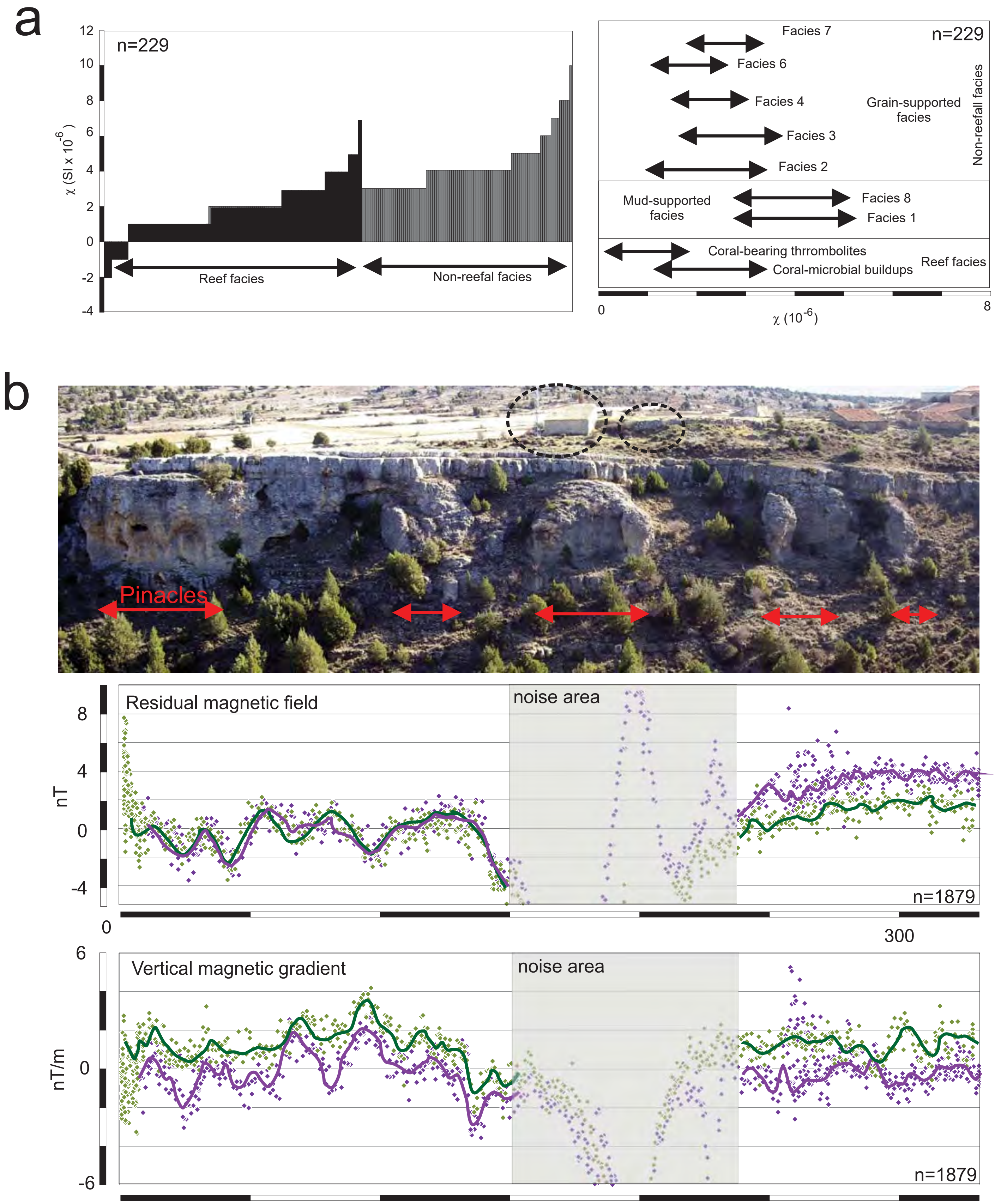
a
n=229
12
10
8
6
4
2
0
-2
-4
χ (SI x 10^-6)
Reef facies
Non-reefal facies
Facies 7
n=229
Facies 6
Facies 4
Grain-supported facies
Non-reefall facies
Facies 3
Facies 2
Mud-supported facies
Facies 8
Facies 1
Coral-bearing thrrombolites
Coral-microbial buildups
Reef facies
0
8
χ (10^-6)
b
Pinacles
Residual magnetic field
noise area
nT
8
4
0
-4
n=1879
0
300
6
Vertical magnetic gradient
noise area
nT/m
0
-6
n=1879

Figure 7

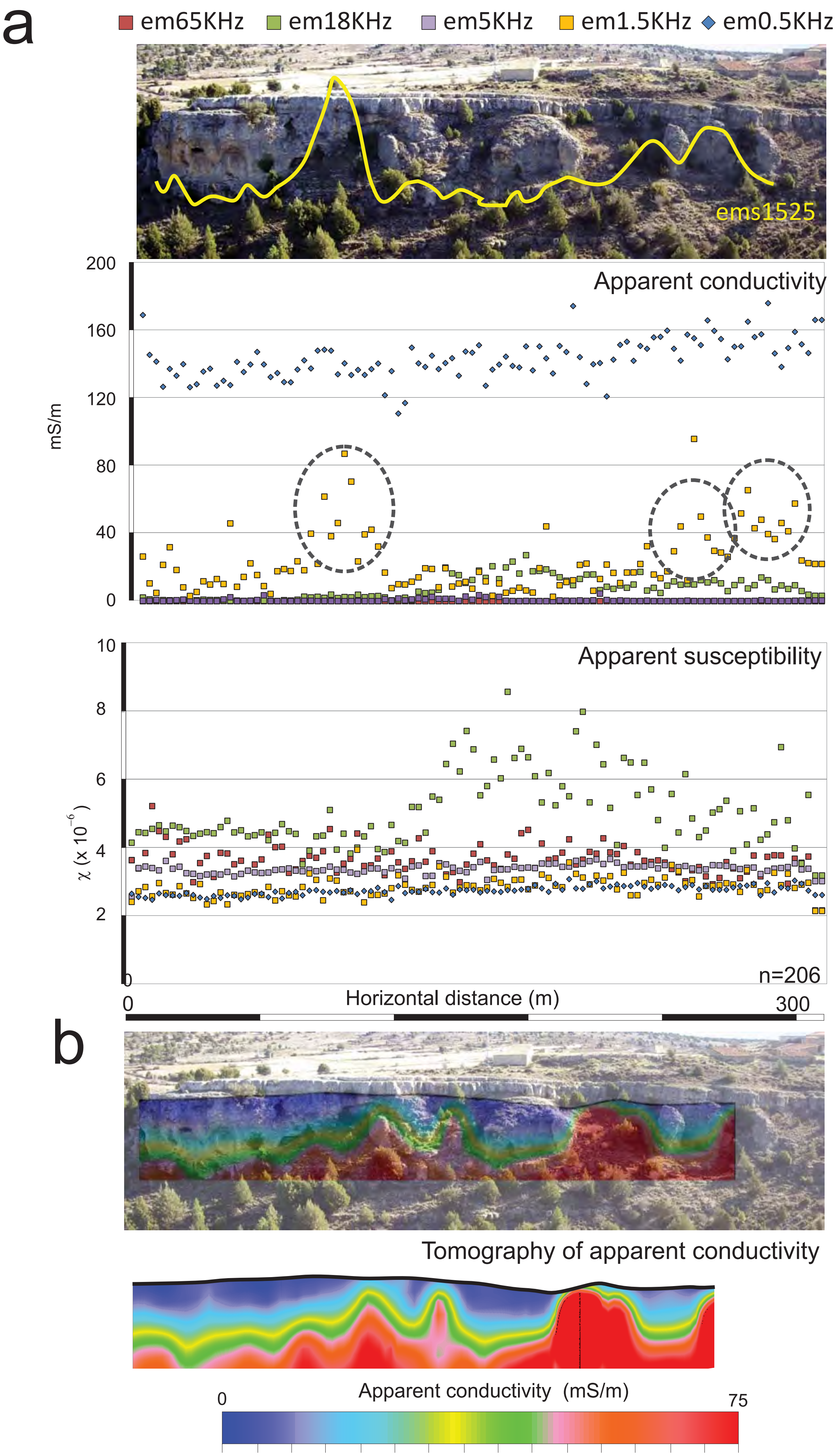
a
em65KHz
em18KHz
em5KHz
em1.5KHz
em0.5KHz
ems1525
Apparent conductivity
mS/m
200
160
120
80
40
0
Apparent susceptibility
χ (x 10⁻⁶)
10
8
6
4
2
0
n=206
Horizontal distance (m)
0
300
b
Tomography of apparent conductivity
Apparent conductivity (mS/m)
0
75

Figure 8.-

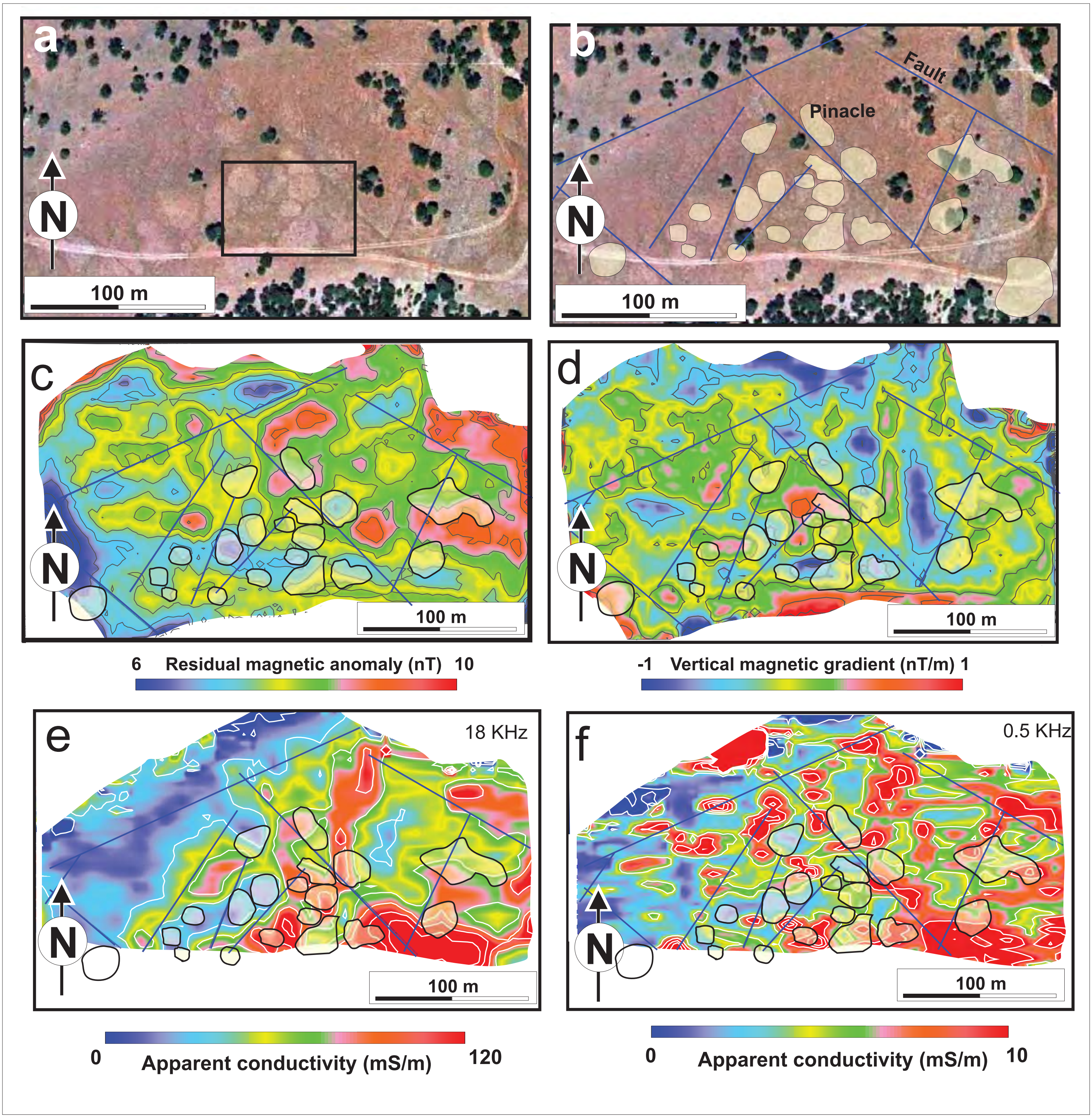

a
100 m
N
b
Fault
Pinacle
100 m
N
c
100 m
N
d
100 m
N
6 Residual magnetic anomaly (nT) 10
-1 Vertical magnetic gradient (nT/m) 1
e
18 KHz
100 m
N
f
0.5 KHz
100 m
N
0 Apparent conductivity (mS/m) 120
0 Apparent conductivity (mS/m) 10

Figure 9

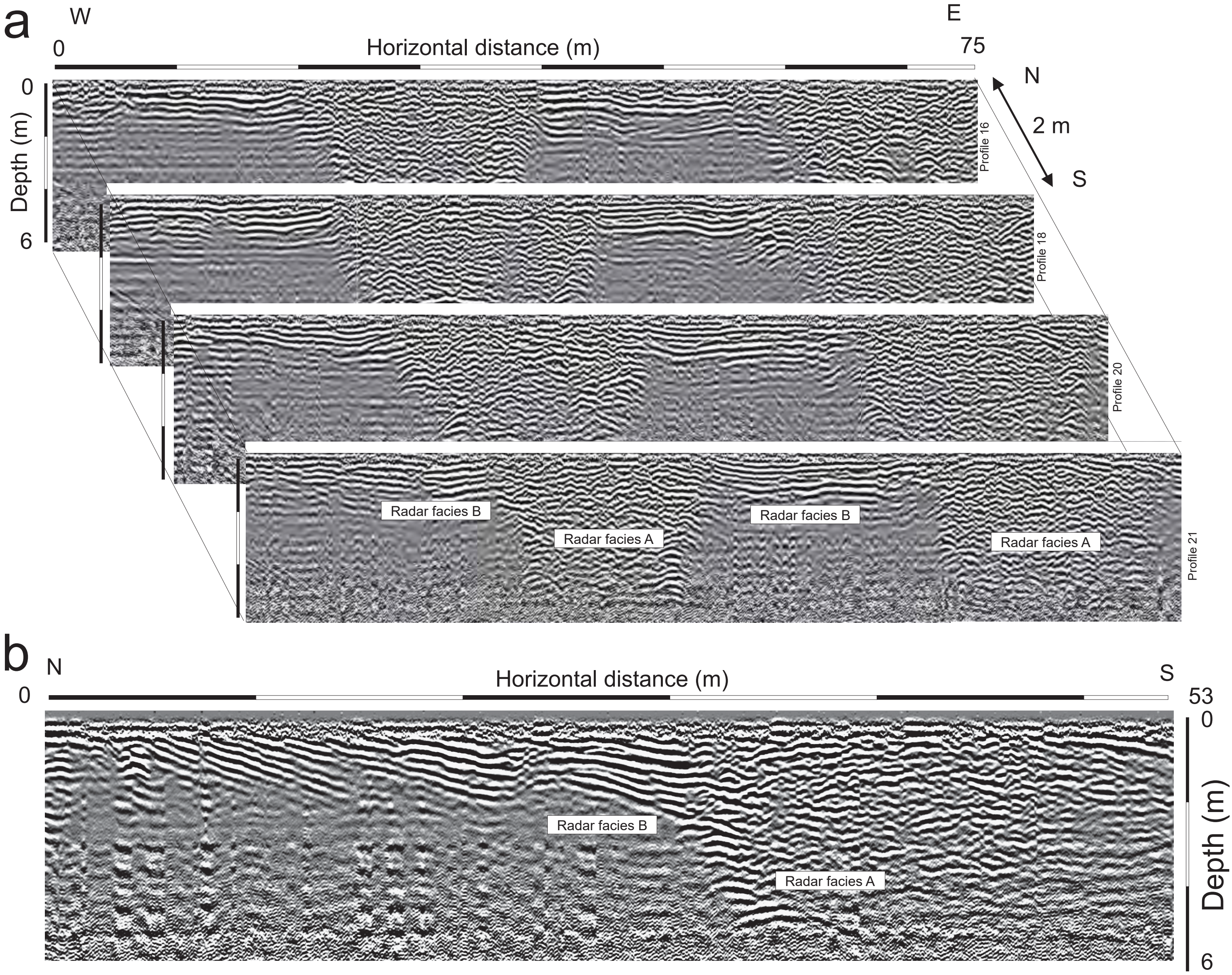
a
W
E
0
Horizontal distance (m)
75
N
2 m
S
0
Depth (m)
6
Profile 16
Profile 18
Profile 20
Radar facies B
Radar facies A
Radar facies B
Radar facies A
Profile 21
b
N
S
0
Horizontal distance (m)
53
Radar facies B
Radar facies A
0
Depth (m)
6

Figure 10

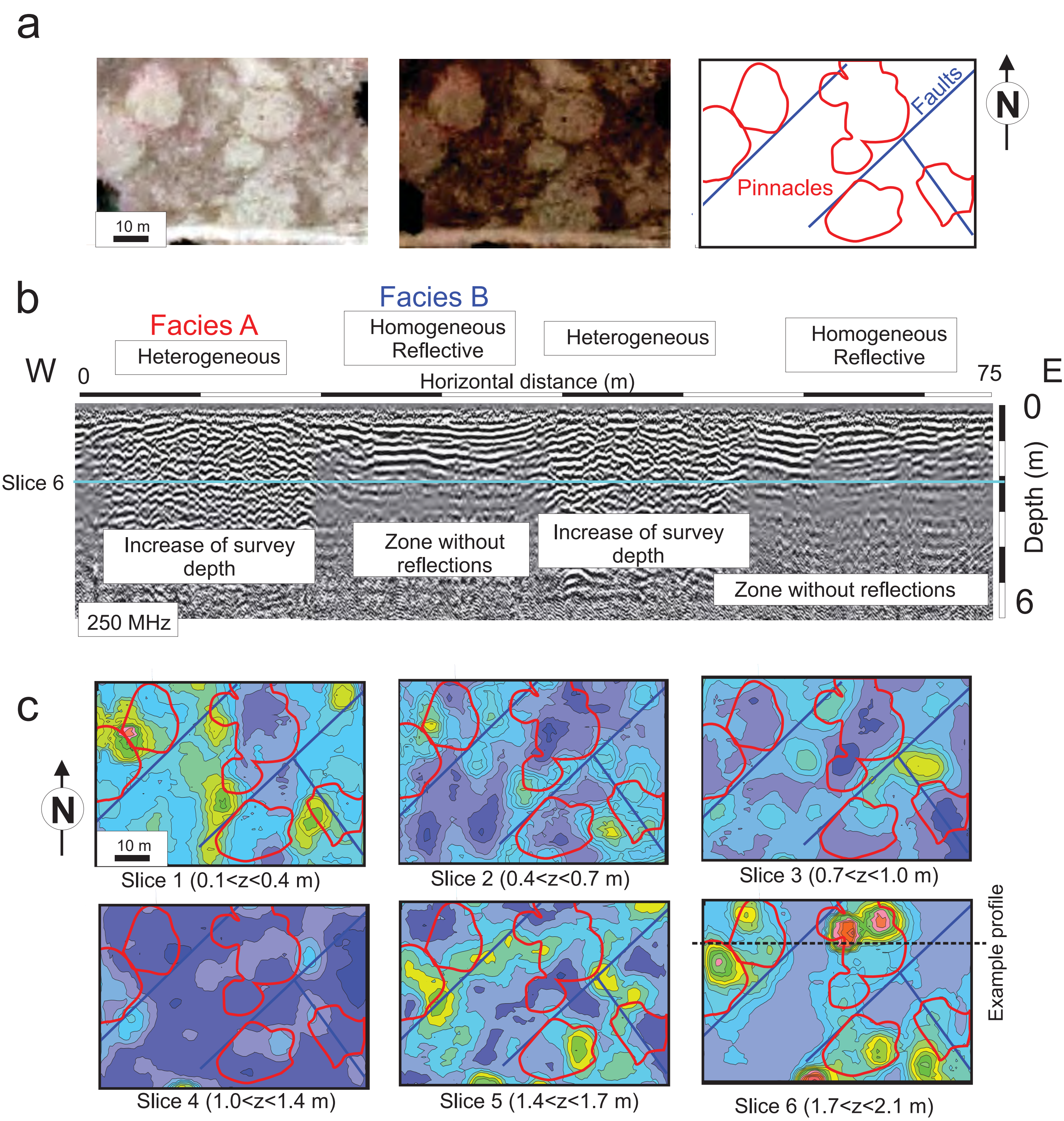
a
10 m
Faults
N
Pinnacles
b
Facies A
Heterogeneous
Facies B
Homogeneous
Reflective
Heterogeneous
Homogeneous
Reflective
W
0
Horizontal distance (m)
75
E
0
Depth (m)
6
Slice 6
Increase of survey depth
Zone without reflections
Increase of survey depth
Zone without reflections
250 MHz
c
N
10 m
Slice 1 (0.1<z<0.4 m)
Slice 2 (0.4<z<0.7 m)
Slice 3 (0.7<z<1.0 m)
Slice 4 (1.0<z<1.4 m)
Slice 5 (1.4<z<1.7 m)
Slice 6 (1.7<z<2.1 m)
Example profile

Figure 11

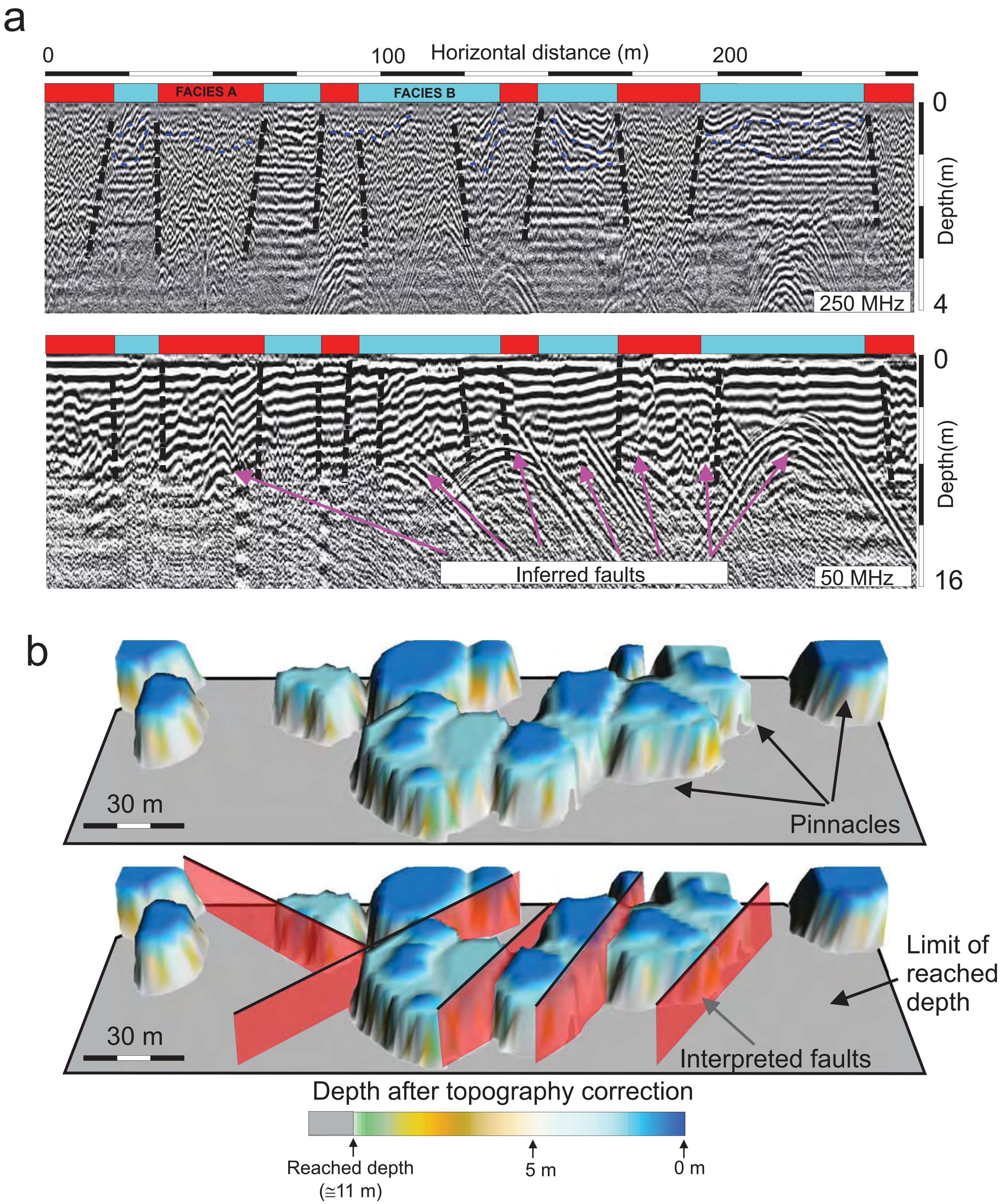
a
0
100
Horizontal distance (m)
200
FACIES A
FACIES B
0
Depth(m)
4
250 MHz
0
Depth(m)
16
Inferred faults
50 MHz
b
30 m
Pinnacles
30 m
Limit of reached depth
Interpreted faults
Depth after topography correction
Reached depth (≅11 m)
5 m
0 m

Figure 12

Geophysical survey	Studied areas: *Structural platform*	Studied areas: *Cliff*	Applicability
Magnetometry			
Residual magnetic anomaly	Pinnacle reefs: usually negative anomalies	Pinnacle reefs: low values	Not useful for univocal identification of facies and faults in subsurface
Vertical magnetic gradient	Pinnacle reefs: usually negative anomalies Faults: lineaments of dipoles	Anomalies at the contact between pinnacle reefs and non-reefal facies	
Magnetic susceptibility			
	-	Pinnacle reefs: negative values (highest values in mud-supported non-reefal facies)	-
EM			
Apparent susceptibility	No clear relationship with facies	No clear relationship with facies	Not useful for univocal identification of facies and faults in subsurface
Apparent conductivity	Non-reefal facies: positive anomalies	Non-reefal facies: positive values and positive peaks in tomography	
GPR			
Profiles	Pinnacle reefs: radar facies A (heterogeneous reflective, increase of survey depth) Non-reefal facies: radar facies B (homogeneous reflective) Faults: hyperbolic anomalies	-	Useful for identification of facies and faults in subsurface
TWT slices	Pinnacle reefs: positive anomalies at deep conditions. Faults: anisotropy (rectilinear contacts) of external envelopes of positive anomalies	-	